

Article

Directional Oxidation of Pyrite in Acid Solution

Jiling Feng ^{1,2}, Hua Tian ^{1,2}, Yaling Huang ^{1,2}, Zhiying Ding ^{1,2,*} and Zhoulan Yin ^{1,2}

¹ School of Chemistry and Chemical Engineering, Central South University, Changsha 410083, China; fengjlcsu@163.com (J.F.); tianxlu@yeah.net (H.T.); yelinahuang@163.com (Y.H.); xhli@csu.edu.cn (Z.Y.)

² Hunan Provincial Key Laboratory of Efficient and Clean Utilization of Manganese Resources, Central South University, Changsha 410083, China

* Correspondence: zy.ding@csu.edu.cn; Tel.: +86-731-88-879-616

Received: 31 October 2018; Accepted: 20 December 2018; Published: 22 December 2018



Abstract: This study aimed to investigate the oxidation mechanism of pyrite crystallographic direction by cutting pyrite samples to expose their (100), (110), and (111) planes. Differences in the oxidation rates of pyrite planes in acid solution were determined. The morphological changes of pyrite were evaluated by scanning electron microscopy and hyperdepth-3D microscopy. The oxidation products of pyrite were examined by Raman spectroscopy and X-ray photoelectron spectroscopy. Results showed that the aqueous oxidation of pyrite produced Fe(OH)₃, Fe₂O₃, Fe₂(SO₄)₃, and S₈ on the surface. Moreover, the morphologies of corrosion patterns differed from one crystal plane to another: square, rectangular, and triangular etch pits were found on the (100), (110), and (111) planes, respectively. The corrosion patterns reflected the symmetrical arrangement of the crystallographic planes in the lattice on which they formed.

Keywords: pyrite; crystallographic direction; oxidation; etch pits

1. Introduction

Pyrite, accompanied with other sulfide ores, is considered the most abundant metal sulfide in the Earth's crust and is frequently found in massive hydrothermal deposits, igneous rocks, and sedimentary beds [1–3]. Natural pyrite contains many heavy metals, such as Ag, Au, Cd, Co, Cu, Mo, Ni, Pb, Se, Sb, Sn, Te, and Zn [4]. Thus, pyrite oxidation usually releases many heavy-metal ions. Furthermore, pyrite oxidation involves water and oxygen consumption, in which sulfuric acid forms and acid mine (or acid rock) drainage (AMD or ARD) subsequently occurs. AMD or ARD has become a long-term environmental problem, affecting the ecological environment through the dissolution of rocks, acidification of aquifers, and mobilization of heavy metals. Pyrite oxidation has attracted considerable attention in the past decades [5–10]. For example, surface oxidation of pyrite aids in the extraction of valuable metals from pyrite deposits. Meanwhile, pyrite oxidation in acid solutions, which is the main source of AMD, should be investigated. However, the oxidation mechanism of pyrite remains unclear. The reported results and conclusions do not conform with oxidation mechanism and kinetics [11]. In general, several intermediate products, such as S₂O₃²⁻, S⁰, and HSO₄⁻, are probably formed during pyrite oxidation [12–15]. S₈, Fe₂O₃, and Fe(OH)₃ are also found [16]. Accordingly, this study aimed to systematically investigate the surface oxidation of pyrite to understand its oxidation mechanism and to find means to reduce the source of AMD.

The crystal structure of pyrite resembles that of NaCl. Pyrite belongs to the crystallographic space group Pa $\bar{3}$ [17]. Dumbbell-shaped disulfide ions (S₂²⁻) and Fe atoms occupy the Cl and Na positions, respectively. S₂²⁻ is located at the center of the cubes and at the midpoints of the cube edges. Each S atom is coordinated with three Fe and another S atom, and each Fe atom bonds with six S atoms in a tilted octahedron [18]. Naturally-exposed crystal planes, such as cubic (100), octahedral (111), and pyritohedral (210) planes, are some low miller index facets [19]. Few studies have focused on

crystal direction properties during pyrite oxidation. Sit et al. [20] investigated the interaction of pyrite (100) plane with water and oxygen molecules by using density functional theory (DFT). Zhu et al. [21] evaluated the oxidation behavior of naturally existing (100), (111), and (210) planes by conducting DFT calculations. All these studies provide detailed information about the atomic structure of crystal directions and some possibilities in investigating the surface changes during pyrite oxidation.

In the present work, the directional oxidation rate and morphologies of pyrite surface were investigated. Raman spectroscopy and X-ray photoelectron spectroscopy (XPS) were used to detect the surface oxidation products. The results on surface morphology can provide a complete understanding of pyrite oxidation.

2. Sample and Methods

2.1. Sample Preparation

Lump pyrite samples with approximately 1 cm³ and 4–6 g weight used in this study were natural cubic pyrite obtained from Hunan Province, China. The samples were cut by using a diamond saw parallel to the (100), (110), and (111) planes and were mounted with epoxy resin, where only the cut surfaces are exposed [22]. Before each experiment, the cut surfaces were polished with abrasive paper and diamond paste, washed with deionized water, and ultrasonically cleaned in ethanol for 30 min to remove any soluble impurities. The polished samples were placed in a glove box (Mikrouna Super 1220/750/900, Mikrouna, Shanghai, China) to avoid oxidation in air. The chemical composition of pyrite samples was analyzed by using an X-ray fluorescence (XRF, Shimadzu-1800, Shimadzu Corp., Kyoto, Japan) at 40 kV and 95 mA. The results listed in Table 1 show that the sample is a typical pyrite with 44.86% Fe and 44.06% S, which slightly deviates from theoretical composition (Fe 46.6%, S 53.4%). The main impurities are O, Si, Al, K, Ti, Ca, Zn, Ru, and Mg, all in trace amounts. The content of O accounting for 8.45% is the highest among the impurities, which may be due to the surface oxidation or S defect in the lattice.

Table 1. Chemical analysis for the pyrite sample.

Element	Fe	S	O	Si	Al	K	Ti	Ca	Zn	Ru	Mg	P	Ni	Cr
Composition (wt%)	44.86	44.06	8.45	1.07	0.72	0.33	0.12	0.09	0.09	0.09	0.07	0.02	0.02	0.01

2.2. Experimental

The matching surfaces of the (100), (110), and (111) planes were used in the experiments. Oxidation experiments in acid solution were conducted at room temperature. The pyrite sample was placed in an Erlenmeyer flask filled with 250 mL of 1 mol/L H₂SO₄ and 10 mL of 9.9 mol/L H₂O₂. The samples were removed and were washed with deionized water and ethanol at certain interval. After drying at room temperature, the morphology changes of samples were monitored by using a scanning electron microscopy (SEM) (Jeol JSM-6490LV, Jeol Ltd., Tokyo, Japan) at a resolution less than 3 nm (30 kV, high vacuum, tungsten filament, secondary electron). The surface element was analyzed by using an energy-dispersive spectrometer (EDS).

A hyperdepth-3D microscopy system (Keyence VHX-5000, Keyence, Osaka, Japan) was used to measure the depth and volume of etching pits on the pyrite surfaces under 500×. The hyperdepth-3D microscopy system has a super high-resolution of z axis of ±1 μm. Autofocus can be realized in 3D directions. The specific steps are expressed as follows: three to five different areas were selected for observation under the hyperdepth-3D microscopy system for each sample. A total of 5–8 etching pits were selected in each region, in which their depth and volume are measured, and their average values are obtained.

The concentration of the total Fe ions (Fe³⁺ and Fe²⁺) was determined by using an inductively-coupled plasma optical emission spectrometer with a Perkin–Elmer Optima 5300 DV

(Perkin–Elmer, Inc., Waltham, MA, USA). Plasma power was 1300 W by using CHNS mode and TCD detector.

Raman spectra data were recorded by using a Renishaw inVia (1800) instrument. The power of He–Ne laser is 50 mW, and laser wavelength is 532 nm. The exposure time is 10 s, which is cumulative three times. The analyzed surface size is approximately 2 mm.

XPS (ESCALAB250Xi, ThermoFisher-VG Scientific, Waltham, MA, USA) analysis was conducted by using a Thermo Scientific Escalab-250 instrument. Al-K α X-ray (1486.6 eV), which is used as the source of radiation, was operated at 150 W (15 kV, 10 mA) and irradiating spot size of 500 μm on the pyrite surface. The depth of surface information is approximately 10 nm. The best vacuum is greater than 5×10^{-10} mbar at room temperature. The C_{1s} spectrum of peak at 284.8 eV was used to correct the data. XPS data were fitted in XPSPEAK4.0 software.

3. Result and Discussion

3.1. Pyrite Surface Characterization

The morphology of freshly polished pyrite surface is shown in Figure 1. Generally, the surface of pyrite is smooth and flat. Several small black spots are occasionally observed, which are probably due to some impurities or defects on the pyrite surface. As shown in Figure 1, the element compositions of fresh pyrite surface are Fe (45.79%) and S (54.21%) with high purity.

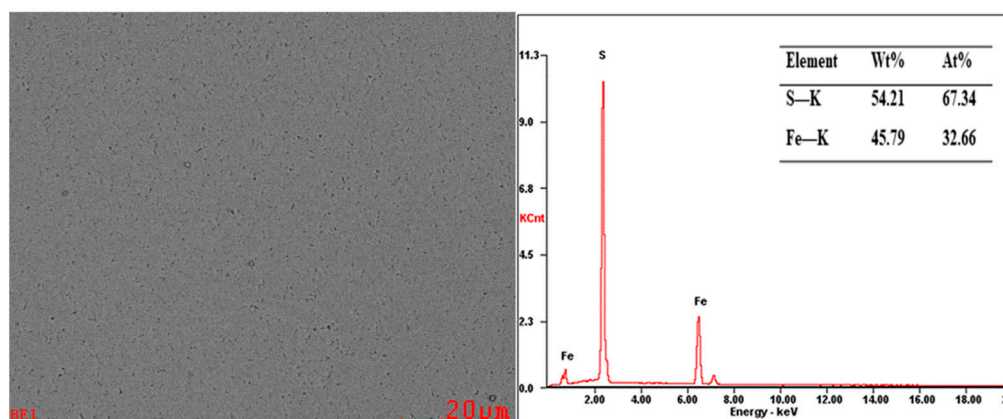


Figure 1. Electron microprobe characterization of a polished pyrite surface.

3.2. Surface Topography Change

Pyrite samples were removed from the reaction vessel after oxidation for four or eight days. Then, the corrosion patterns on the surfaces were observed. Different etching pits were observed on different crystal directions. Figure 2 shows the typical etching pits on the exposed (100), (110), and (111) pyrite surfaces after oxidation for four days. Figure 2a shows that the etching pits are generally square on the (100) plane. Rectangle patterns appear on the (110) plane, as shown in Figure 2b, and the etching pits on the (111) plane are triangular, as shown in Figure 2c. These etching pits usually aggregate together. The etching pits are obvious after oxidation for eight days, as shown in Figure 3. The etching pits on the (110) plane are linked together to exhibit elongated pits. These etching pits reflect the symmetrical arrangement of crystallographic planes in the lattice. The point group of the crystal can be obtained when all etching pits on different directions of the same crystal are combined. The symmetries of the (100), (110), and (111) planes are 4 mm, 2 mm, and 3 mm, respectively. The etching pits in all directions have the same symmetry. The same results are found in olivine and quartz [23]. These results indicate that the corrosion patterns are closely related to the symmetry of the crystal structure.

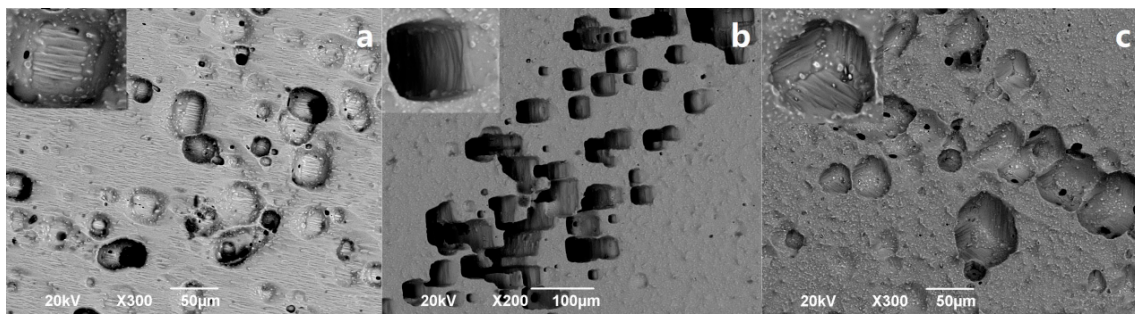


Figure 2. Corrosion patterns on different crystal directions after four days: (a) (100); (b) (110), and (c) (111).

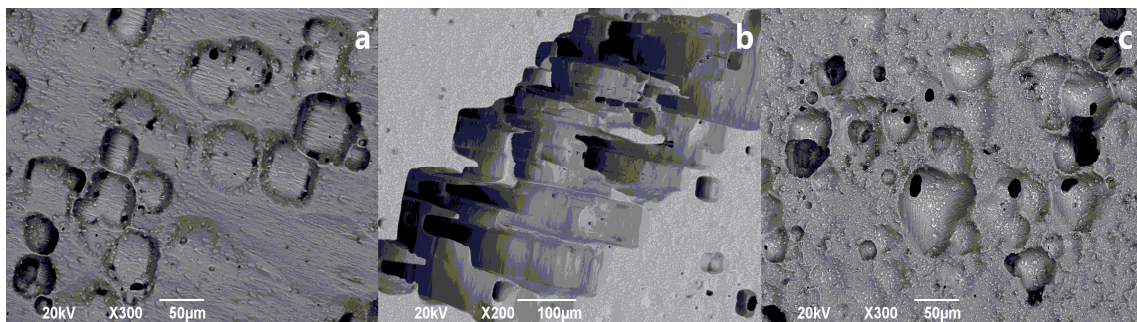


Figure 3. Corrosion patterns on different crystal directions after eight days: (a) (100); (b) (110), and (c) (111).

3.3. Depth and Volume Analysis of Etching Pits

Figure 4a shows the depth changes of etching pits in different planes with time. As shown in Figure 4a, the depth of etching pits increases with time. The depth of etching pits on the (110) plane is larger than that on the (100) and (111) planes. However, the depth of etching pits cannot accurately reflect the oxidation rate because it is related to the density and size of the pits. Then, their volumes are investigated, where different crystal directions have different volumes, as shown in Figure 4b. The volume of etching pits on the (110) plane is the largest, and the volumes of (100) and (111) planes have a small difference. Moreover, the pits grow deep with a small number on the (110) plane. The pits on (100) and (111) planes are small and many.

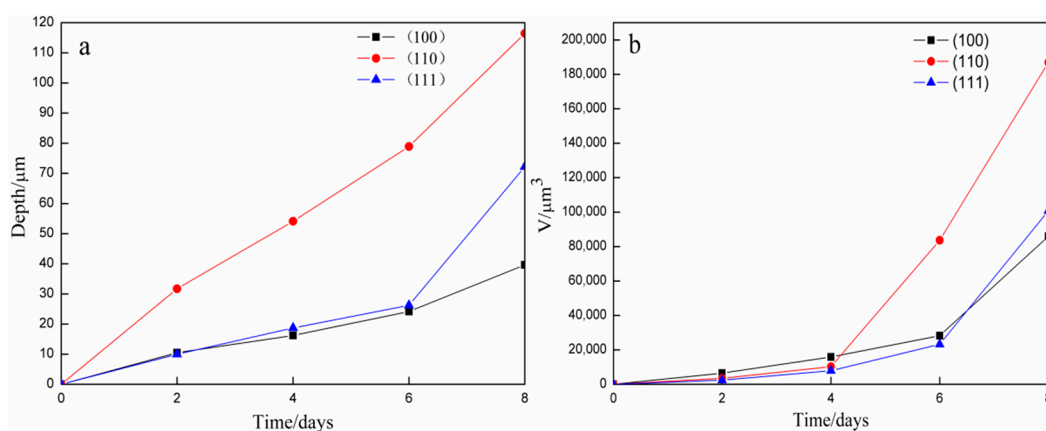


Figure 4. Crystal direction depth and volume changes of etching pits. (a) Depth changes, and (b) volume changes.

3.4. Fe Ion Concentration

Considering the incomplete statistics of etching pits, the concentrations of “total iron” ion were measured in different crystal directions. Figure 5 shows the variation of the “total iron” concentration with time. This figure indicates that different oxidation rates are observed in different crystal directions. The (111) plane shows a higher oxidation rate compared with the (100) and (110) planes. The directional oxidation rate is $r_{(111)} > r_{(110)} > r_{(100)}$. This finding agrees with the results of Ndlovu and Monhemius [22] and is probably due to the difference in geometric arrangement of atoms in different crystal directions. The atomic arrangement of the pyrite (111) plane is $-S-S-S-$ or $-Fe-Fe-Fe-$, and the (100) plane is $-Fe-S-S-Fe-$. The S-S bond in pyrite is weaker than that of the Fe-S bond [24]. Therefore, the (100) plane is more stable. The results indicate that the surface atomic arrangement is important for the physical and chemical behavior of pyrite. Moreover, crystal growth theory (periodic bond chain (PBC) theory) describes that the morphology of crystals is obtained from the geometrical characteristics of the internal structure of crystals and the energy of particles. A PBC is an uninterrupted bond chain with periodic repetition of the strongest bond in a certain direction of crystallization. The plane refers to the F surface when more than two PBCs are parallel to a certain plane, in which its mesh is dense and flat and its growth rate is small. The plane refers to the S surface when only one PBC is parallel to it, which has a small and few secondary directions on the crystal. This plane is also called the stepped face. The plane refers to the K surface when no PBC is parallel to it, which is also called the kinked face. Its growth rate is the fastest and easier to disappear [25]. In pyrite, the Fe-S bond is stronger than that of S-S bond. Two periodic Fe-S bond chains are parallel to the (100) plane, which belong to the F surface and indicate its stable property. The (110) plane has one parallel PBC, which shows a fast oxidation rate. Meanwhile, the (111) plane without any parallel PBC exhibits a faster oxidation rate. This theory perfectly explains our experimental results.

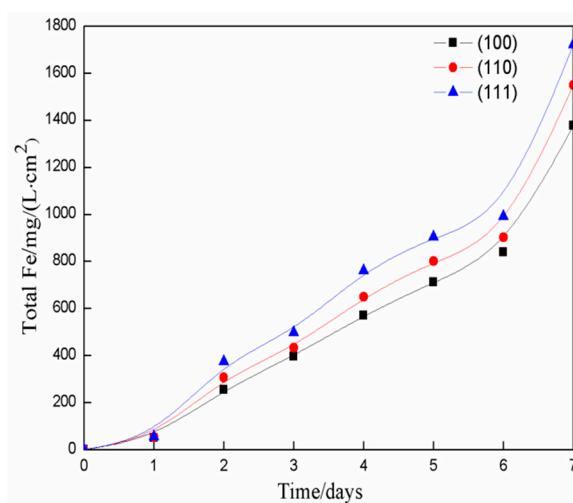
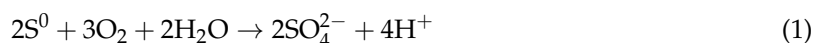


Figure 5. “Total iron” concentration in acid solution with time.

3.5. Raman Spectra Analysis

Raman spectra on different crystal directions of pyrite were measured before and after oxidation in acid solution to obtain the oxidation products of pyrite, as shown in Figure 6. Before oxidation, three peaks are found on the (100), (110), and (111) pyrite planes, which are located at 342 , 380 , and 430 cm^{-1} , respectively. These peaks can be attributed to the deformation vibration of S-S and stretching vibration peak of Fe-S and S-S. New peaks appear or some peaks disappear after eight days. As shown in Figure 6a, the stretching vibrational peaks of S-S disappear, and other products on the surface are not detected through Raman spectroscopy, which show that the S-Fe bond is more stable than that of the S-S bond. For the (110) plane in Figure 6b, new peaks at 226 and 410 cm^{-1} appear, which can be ascribed to $Fe(OH)_3$. The weak peak at approximately 244 cm^{-1} belongs to the Fe-O stretching

vibrations of Fe(OH)₃ or S. The peak at 290 cm⁻¹ is the symmetric stretching vibration of the Fe–O bond of Fe₂O₃. The weak peak at 609 cm⁻¹ is the bending vibration of the Fe–O bond of Fe₂O₃ or Fe(OH)₃. This spectrum shows that Fe₂O₃ and Fe(OH)₃ are definitely formed on the pyrite surface, which agrees with the results of Tu et al. [16]. However, the peak of S is not evident, which is probably because S is oxidized to sulfate. The reaction equation is expressed as Equation (1)



The Raman spectra for the pyrite (111) plane in Figure 6c exhibit two weak and broad peaks. The first peak is located at 220–234 cm⁻¹, which is possibly due to the mixture of Fe(OH)₃ and S on the pyrite surface. The second peak is located at approximately 280 cm⁻¹, which can be ascribed to Fe₂O₃.

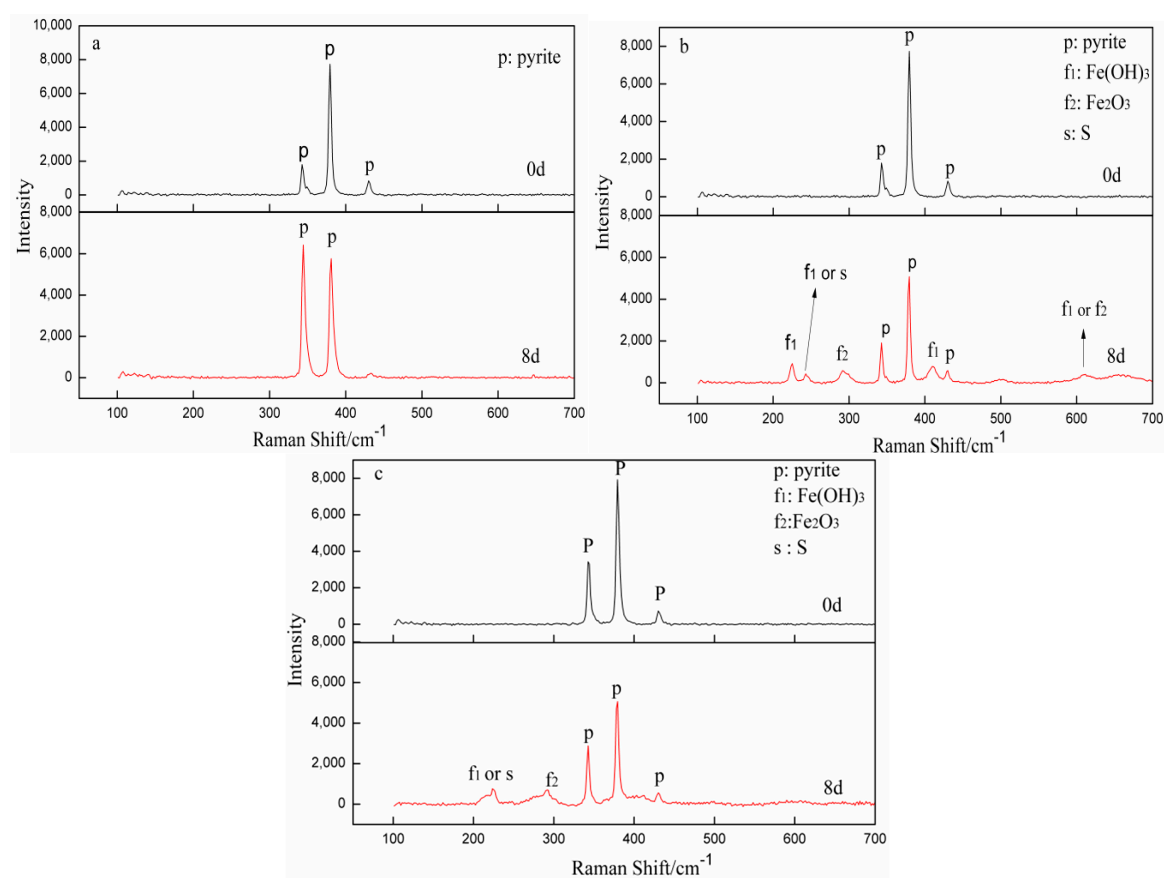


Figure 6. Raman spectrum on the crystal directions of pyrite: (a) (100); (b) (110), and (c) (111).

3.6. XPS Analysis

The spectra of pyrite (100), (110), and (111) are shown in Figures 7 and 8. The common binding energies are determined based on the literature in Table 2. As shown in Figure 7a, the S(2p) peaks of pyrite are concentrated on 162.3, 163.4, and 168.5 eV. The major peak at 162.3 eV is assigned to the disulfide of lattice pyrite [16,26]. The peak at 163.4 eV is S₈ [7,16]. The small peak at 168.5 eV is attributed to Fe₂(SO₄)₃, which shows that the pyrite surface is slightly oxidized by air. The Fe(2p) peaks of pyrite are shown in Figure 7b. The peaks at 707.2 eV and 720.0 eV are Fe(2p_{3/2}) and Fe(2p_{1/2}) of pyrite(FeS₂), respectively [16,26,27]. The other weak peaks at 710.7, 713.2, 724.7, and 732.7 eV belong to Fe(OH)₃, Fe₂(SO₄)₃, and Fe₂O₃ [16,26]. The peak at 732.7 eV is the satellite of Fe₂O₃ [26,28]. The S(2p) spectra in Figure 8a are similar to those of primitive pyrite but with slightly broader peaks. Figure 8a shows the S(2p) peaks of pyrite (100), (110), and (111) planes after oxidation for eight days. The primary peak with a binding energy of 168.5 eV assigned to Fe₂(SO₄)₃ remarkably increases on the (111) plane,

indicating that the oxidation rate of (111) plane is fast. This finding is consistent with the result of Raman spectra analysis.

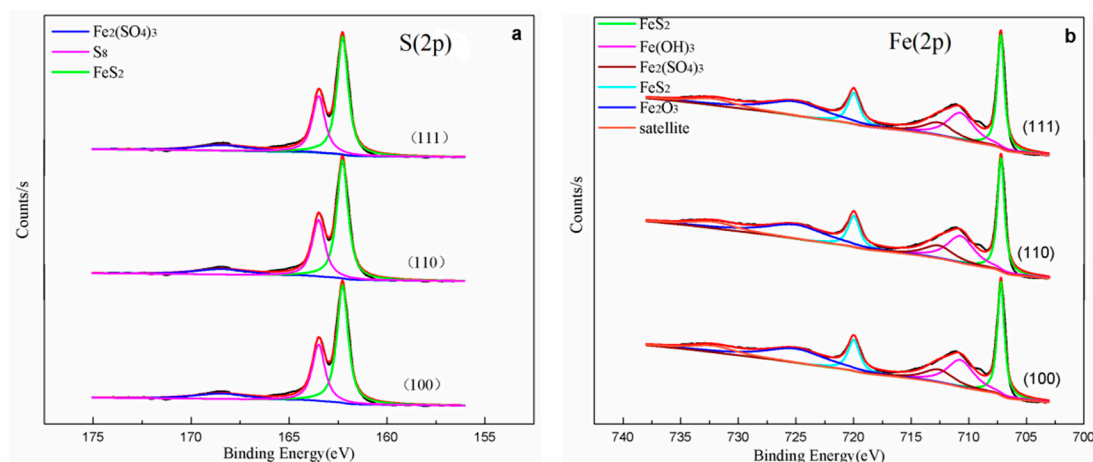


Figure 7. XPS spectra of pyrite (100), (110), and (111): S(2p) (a), and Fe(2p) (b).

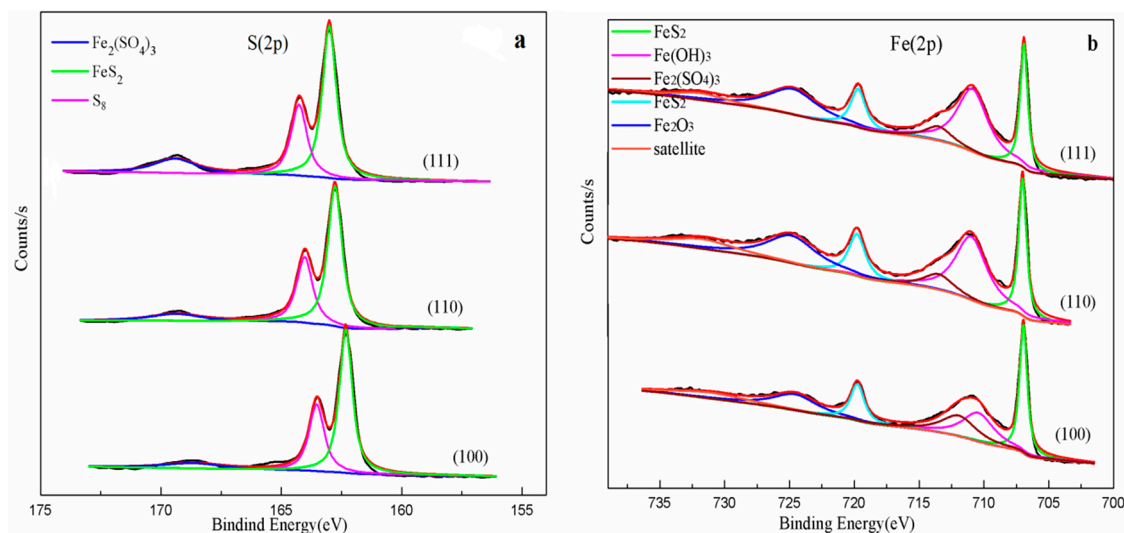


Figure 8. XPS spectra of pyrite (100), (110) and (111) after oxidation for eight days: S(2p) (a) and Fe(2p) (b).

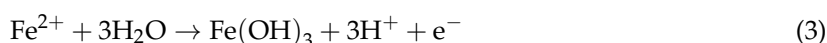
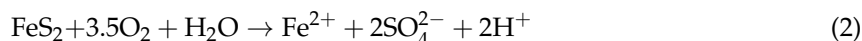
Table 2. Binding energy of Fe(2p) and S(2p) after oxidation for eight days.

Spectrum	Unreacted Pyrite	Binding Energy(eV) (2p)			Species
		(100)	(110)	(111)	
S _{2p}	162.3(2p _{3/2})	162.3(2p _{3/2})	162.3(2p _{3/2})	162.3(2p _{3/2})	FeS ₂ [16,26]
	163.4(2p _{3/2})	163.5(2p _{3/2})	163.5(2p _{3/2})	163.5(2p _{3/2})	S ₈ [7,16]
	168.5(2p _{3/2})	168.6(2p _{3/2})	168.6(2p _{3/2})	168.4(2p _{3/2})	Fe ₂ (SO ₄) ₃ [16,26]
Fe _{2p}	707.2(2p _{3/2})	707.0(2p _{3/2})	707.0(2p _{3/2})	706.9(2p _{3/2})	FeS ₂ [16,26,27]
	720.0(2p _{1/2})	719.8(2p _{1/2})	720.0(2p _{1/2})	719.7(2p _{1/2})	
Satellite	710.7(2p _{3/2})	710.3(2p _{3/2})	711.1(2p _{3/2})	710.8(2p _{3/2})	Fe(OH) ₃ [16]
	724.7(2p _{1/2})	724.7(2p _{1/2})	724.8(2p _{1/2})	724.7(2p _{1/2})	Fe ₂ O ₃ [26,28]
	732.7(2p _{1/2})	732.2(2p _{1/2})	732.1(2p _{1/2})	731.8(2p _{1/2})	Fe ₂ (SO ₄) ₃ [26]
	713.2(2p _{3/2})	713.2(2p _{3/2})	713.5(2p _{3/2})	713.5(2p _{3/2})	

Figure 8b shows the Fe(2p) peaks of (100), (110), and (111) planes after oxidation for eight days compared with the primitive pyrite. The peak at 710.9 eV is considered to be Fe(2p_{3/2}) of

Fe(OH)₃. The peak at 713.2 eV is the Fe(2p_{3/2}) of Fe₂(SO₄)₃. These findings are in agreement with the abovementioned S(2p) spectra results. The peak at 724.7 eV is attributed to Fe(2p_{1/2}) of Fe₂O₃. The Fe(2p_{1/2}) of Fe₂O₃ satellite binding energy is 732.2 eV [26]. The XPS spectra of the (110) and (111) planes are similar. However, the Fe(2p_{3/2}) peak of FeS₂ on the (111) plane is weaker than that of (110) and (100) planes. The Fe(2p_{1/2}) peak of Fe₂O₃ is obvious on the (111) plane. These conditions verify that the oxidation rate of the (111) plane is faster than that of the (110) plane. Meanwhile, Fe(OH)₃ and Fe₂(SO₄)₃ are found on the (110) and (111) planes. Fe₂(SO₄)₃ was detected based on the XPS spectra, which is different from the Raman spectra.

Based on the Raman spectroscopy and XPS analyses, the following reactions are proposed to have occurred:



4. Conclusions

This work investigated the differences in the directional oxidation rates of pyrite in acid solution, which order is $r_{(111)} > r_{(110)} > r_{(100)}$. The (110) plane appears more reactive than that the (100) plane. These conclusions can be explained by the surface atomic arrangement. The (111) plane is –S–S–S– or –Fe–Fe–Fe–, and the (110) plane is –Fe–S–S–Fe–. Considering that the S–S bond is weaker than the Fe–S bond, the (100) plane is more stable. Different etching pits formed on different crystal directions. A square etching pit was formed on the (100) plane. Rectangular and triangular etching pits formed on the (110) and (111) planes, respectively. The different corrosion patterns suggested that the shapes of etching pits were consistent with the symmetry of the crystal direction. Raman spectra and XPS results further indicated that pyrite was oxidized under acid condition to form Fe₂O₃, Fe(OH)₃, Fe₂(SO₄)₃, and S.

Author Contributions: J.F. and Z.D. proposed and organized the project. J.F., H.T., and Y.H. discussed and designed and performed the experiment. J.F. and H.T. analyzed and interpreted the data. J.F. wrote the main manuscript. Z.D. and Z.Y. revised the main manuscript. All the authors discussed the study.

Funding: This research was funded by the National Key Basic Research Program of China (grant no. 2014CB643401), National Natural Science Foundation of China (grant no. 51404299), and the Hunan Provincial Science and Technology Plan of China (grant no. 2016TP1007).

Conflicts of Interest: The authors declare no conflict of interest.

References

1. Nesbitt, H.W.; Muir, I.J. X-ray photoelectron spectroscopic study of a pristine pyrite surface reacted with water vapour and air. *Geochim. Cosmochim. Acta* **1994**, *58*, 4667–4679. [[CrossRef](#)]
2. Rickard, D. *Pyrite: A Natural History of Fool's Gold*; Oxford University Press: Oxford, UK, 2015.
3. Tauson, V.L.; Kravtsova, R.G.; Grebenshchikova, V.I.; Lustenberg, E.E.; Lipko, S.V. Surface typochemistry of hydrothermal pyrite: Electron spectroscopic and scanning probe microscopic data. II. Natural pyrite. *Geochem. Int.* **2009**, *47*, 231–243. [[CrossRef](#)]
4. Abraitis, P.K.; Patrick, R.A.D.; Vaughan, D.J. Variations in the compositional, textural and electrical properties of natural pyrite: A review. *Int. J. Miner. Process.* **2004**, *74*, 41–59. [[CrossRef](#)]
5. Sasaki, K.; Tsunekawa, M.; Ohtsuka, T.; Konno, H. Confirmation of a sulfur-rich layer on pyrite after oxidative dissolution by Fe(III) ions around pH 2. *Geochim. Cosmochim. Acta* **1995**, *59*, 3155–3158. [[CrossRef](#)]
6. Mckibben, M.A.; Barnes, H.L. Oxidation of pyrite in low temperature acidic solutions: Rate laws and surface textures. *Geochim. Cosmochim. Acta* **1986**, *50*, 1509–1520. [[CrossRef](#)]

7. Woods, A.N.B. The surface oxidation of pyrite. *Appl. Surf. Sci.* **1987**, *27*, 437–452.
8. De Leeuw, N.H.; Parker, S.C.; Sithole, H.M.; Ngoepe, P.E. Modeling the Surface Structure and Reactivity of Pyrite: Introducing a Potential Model for FeS₂. *J. Phys. Chem. B* **2000**, *104*, 7969–7976. [[CrossRef](#)]
9. Hung, A.; Muscat, J.; Yarovsky, I.; Russo, S.P. Density-functional theory studies of pyrite FeS₂(100) and (110) surfaces. *Surf. Sci.* **2002**, *513*, 511–524. [[CrossRef](#)]
10. Qiu, G.; Gao, T.; Hong, J.; Tan, W.; Liu, F.; Zheng, L. Mechanisms of arsenic-containing pyrite oxidation by aqueous arsenate under anoxic conditions. *Geochim. Cosmochim. Acta* **2017**, *217*. [[CrossRef](#)]
11. Chandra, A.P.; Gerson, A.R. The mechanisms of pyrite oxidation and leaching: A fundamental perspective. *Surf. Sci. Rep.* **2010**, *65*, 293–315. [[CrossRef](#)]
12. Long, H.; Dixon, D.G. Pressure oxidation of pyrite in sulfuric acid media: A kinetic study. *Hydrometallurgy* **2004**, *73*, 335–349. [[CrossRef](#)]
13. Tu, Z.; Guo, C.; Zhang, T.; Lu, G.; Wan, J.; Liao, C.; Dang, Z. Investigation of intermediate sulfur species during pyrite oxidation in the presence and absence of *Acidithiobacillus ferrooxidans*. *Hydrometallurgy* **2016**, *167*, 58–65. [[CrossRef](#)]
14. Kelsall, G.H.; Yin, Q.; Vaughan, D.J.; England, K.E.R.; Brandon, N.P. Electrochemical oxidation of pyrite (FeS₂) in aqueous electrolytes. *J. Electroanal. Chem.* **1999**, *471*, 116–125. [[CrossRef](#)]
15. Sun, H.; Chen, M.; Zou, L.; Shu, R.; Ruan, R. Study of the kinetics of pyrite oxidation under controlled redox potential. *Hydrometallurgy* **2015**, *155*, 13–19. [[CrossRef](#)]
16. Tu, Z.; Wan, J.; Guo, C.; Fan, C.; Zhang, T.; Lu, G.; Reinfelder, J.R.; Dang, Z. Electrochemical oxidation of pyrite in pH 2 electrolyte. *Electrochim. Acta* **2017**, *239*, 25–35. [[CrossRef](#)]
17. Paszkowicz, W.; Leiro, J.A. Rietveld refinement study of pyrite crystals. *J. Alloys Compd.* **2005**, *401*, 289–295. [[CrossRef](#)]
18. Vaughan, D.J.; Craig, J.R. *Mineral Chemistry of Metal Sulfides*; Cambridge University Press: Cambridge, UK, 1987; pp. 410–411.
19. Chen, G.Y.; Sun, D.S.; Zhang, L.; Zang, W.S.; Wang, J.; Lu, A.H. Morphogenesis of pyrite. *Geoscience* **1987**, *1*, 60–76.
20. Sit, P.H.; Cohen, M.H.; Selloni, A. Interaction of Oxygen and Water with the (100) Surface of Pyrite: Mechanism of Sulfur Oxidation. *J. Phys. Chem. Lett.* **2012**, *3*, 2409–2414. [[CrossRef](#)]
21. Zhu, J.; Xian, H.; Lin, X.; Tang, H.; Du, R.; Yang, Y.; Zhu, R.; Liang, X.; Wei, J.; Teng, H.H. Surface structure-dependent pyrite oxidation in relatively dry and moist air: Implications for the reaction mechanism and sulfur evolution. *Geochim. Cosmochim. Acta* **2018**, *228*, 259–274. [[CrossRef](#)]
22. Ndlovu, S.; Monhemius, A.J. The influence of crystal orientation on the bacterial dissolution of pyrite. *Hydrometallurgy* **2005**, *78*, 187–197. [[CrossRef](#)]
23. Zhao, S.; Xu, C.; Zhang, G.; Li, K. Etch Figures Related to the Symmetry and Structure of the Crystal Faces. *Earth Sci.* **2013**, *38*, 211–217.
24. Nesbitt, H.W.; Bancroft, G.M.; Pratt, A.R.; Scaini, M.J. Sulfur and iron surface states on fractured pyrite surfaces. *Am. Mineral.* **1998**, *83*, 1067–1076. [[CrossRef](#)]
25. Wang, W.; Wang, J.; Zhao, S. *Crystal Morphology*; China University of Geosciences Press: Wuhan, China, 2001.
26. Descostes, M.; Mercier, F.; Thromat, N.; Beaucaire, C.; Gautier-Soyer, M. Use of XPS in the determination of chemical environment and oxidation state of iron and sulfur samples: constitution of a data basis in binding energies for Fe and S reference compounds and applications to the evidence of surface species of an oxidized pyrite in a carbonate medium. *Appl. Surf. Sci.* **2000**, *165*, 288–302.
27. Eggleston, C.M.; Ehrhardt, J.J.; Stumm, W. Surface structural controls on pyrite oxidation kinetics; an XPS-UPS, STM, and modeling study. *Am. Mineral.* **1996**, *81*, 1036–1056. [[CrossRef](#)]
28. Sang, Y.L.; Kim, D.H.; Choi, S.C.; Lee, D.J.; Ji, Y.C.; Kim, H.D. Porous multi-walled carbon nanotubes by using catalytic oxidation via transition metal oxide. *Microporous Mesoporous Mater.* **2014**, *194*, 46–51.

